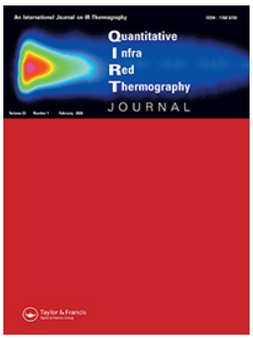

Quantitative InfraRed Thermography Journal

ISSN: 1768-6733 (Print) 2116-7176 (Online) Journal homepage: www.tandfonline.com/journals/tqrt20

The size of source effect for middle- and long-wavelength infrared cameras: assessment by direct measurements and a modulation transfer function approach

Miguel-David Mendez-Bohorquez, Jannik Ebert, Lars Sommerlade, Robert Schmoll & Andreas Kroll

To cite this article: Miguel-David Mendez-Bohorquez, Jannik Ebert, Lars Sommerlade, Robert Schmoll & Andreas Kroll (28 Nov 2025): The size of source effect for middle- and long-wavelength infrared cameras: assessment by direct measurements and a modulation transfer function approach, Quantitative InfraRed Thermography Journal, DOI: 10.1080/17686733.2025.2589712

To link to this article: https://doi.org/10.1080/17686733.2025.2589712

Published online: 28 Nov 2025.

QUANTITATIVE INFRARED THERMOGRAPHY JOURNAL
https://doi.org/10.1080/17686733.2025.2589712

Taylor & Francis
Taylor & Francis Group

The size of source effect for middle- and long-wavelength infrared cameras: assessment by direct measurements and a modulation transfer function approach

Miguel-David Mendez-Bohorquez, Jannik Ebert, Lars Sommerlade, Robert Schmoll and Andreas Kroll

Department of Measurement and Control, University of Kassel, Kassel, Germany

ABSTRACT

Current radiometric calibration procedures for thermal imaging cameras are typically performed for a single calibration geometry. Typical measurement scenarios do not replicate this geometrical condition and the values provided by the devices deviate from the calibration, which is known as the *size-of-source effect* (SSE). This study presents SSE measurements on four thermal imaging cameras: two operating in the long-wavelength infrared (LWIR) range and two in the mid-wavelength infrared (MWIR) range. The results indicate that the SSE increases with temperature as the size of the object deviates from the calibration geometry. The deviations observed in the MWIR cameras were smaller than those in the LWIR cameras. The horizontal modulation transfer function (MTF) was measured and utilised to simulate the response of the optical systems and to compare predictions from an analytical approach with the SSE measurements. Although similar trends are observed between the measured and predicted SSE, the model still fails to reproduce the magnitude of the deviations, possibly due to effects not accounted for by the one-dimensional model, along with additional factors such as scattering. Future work will focus on formulating a 2D model and incorporating additional terms into the system transfer function to account for effects not covered by the measured MTF and to enhance the theoretical prediction of the SSE.

ARTICLE HISTORY
Received 22 May 2024
Accepted 10 November 2025

KEYWORDS
Size-of-source effect; modulation transfer function; thermal imaging cameras; middle wavelength infrared range; long wavelength infrared range

1. Introduction

The *size-of-source effect* (SSE), inherent in any infrared radiation temperature measuring device, is the deviation of the indicated temperature value due to a change in the size of the measured object [1]. If the emissivity is known, this systematic error is considered to be potentially one of the greatest contributions to temperature-measurement uncertainty [2].

For radiation thermometers, extensive research has been conducted to characterise and correct the measurement deviations associated with them. Ohtsuka and Bedford [3] measured the SSE using a dedicated experimental setup designed to minimise data contamination from factors such as spurious reflections and to achieve high measurement resolution. Since the SSE is not represented by large numbers, the authors chose to evaluate it by calculating differences between small quantities rather than small differences between large ones. The contribution of diffraction and scattering phenomena was systematically investigated through mathematical modelling and experimentation, respectively. The authors concluded that SSE is predominantly caused by scattering phenomena, which are not fully addressed by theoretical models restricted to diffraction.

In subsequent studies, the measurement procedures were further analysed [4,5]. Machin and Ibrahim [4] investigated the deviation caused by radiation from the aperture used to vary the source size. It was concluded that for small differences between the source and background, this effect becomes significant, especially when the aperture temperature is higher. For higher differences, the curves corresponding to different radiant temperatures converge, negating this effect. Machin and Sergienko [5] described two different techniques to determine the SSE: the direct and indirect method. Both methods determine the SSE by varying the source size with apertures of

CONTACT Miguel-David Mendez-Bohorquez miguel.mendez@mrt.uni-kassel.de Department of Measurement and Control, University of Kassel, Kassel 34125, Germany

different diameters, but the indirect method employs a central obscuration. According to Bart et al. [6], the primary difference is that the direct method simultaneously measures both the radiation scattered within the nominal field of view and the radiation scattered outside of it, whereas the indirect method only measures the radiation scattered within the nominal field of view. A third technique, known as the scanning method, was proposed by Bart et al. [6], which overcomes the measuring effort of the indirect method. This was extended by Saunders and Hamish [7], who established a relationship between the three methods and enabled the detection of scattering both into and out of the nominal field of view.

Yoon et al. [8] investigated strategies for reducing the SSE through the design of optical components. The authors measured, among other factors, the impact of incorporating additional lenses in the optical path, observing an increase in the SSE associated with internal reflections within the lenses and light scattering patterns, which are also influenced by particles suspended in the air or deposited on the lenses. The performance of optical systems was also investigated, demonstrating that an optimised system with fewer lenses can significantly reduce SSE.

Regarding experimental setups, Hill and Woods [9] addressed the effects associated with the working distance and the type of radiant source used in SSE measurements. The authors reported radiance variations as a function of distance for the sources studied and highlighted the need to include these aspects in the description of the experiments. A system for SSE measurements using the direct method was constructed by Pušnik et al. [10], in which the experimental setup was carefully designed to prevent contamination of the measurements by adjacent effects, such as convective phenomena near the source and heating of the aperture surface.

The investigation of SSE in infrared cameras is a relatively recent development. It was defined in the context of this kind of sensors by the German Association of Engineers (VDI) [1], who provided guidelines on how it should be measured for thermographic cameras. Pušnik et al. [11] studied the SSE for a long-wavelength infrared (LWIR) camera with different aperture geometries placed in front of a Black body and at varying distances between the aperture and the camera. The authors concluded that the SSE is not negligible and should be specified by manufacturers. Schramm et al. [12] measured the SSE for two LWIR cameras and proposed a compensation method based on an image processing approach. The authors found that the SSE affects the measurement uncertainty, and that applying a digital filter reduces temperature deviations, achieving ranges specified by the manufacturer. König et al. [13] also measured the SSE of three LWIR cameras, two with microbolometer sensors and one with a cooled mercury cadmium telluride (MCT) sensor, with a plate radiator at a temperature of 100 °C. The study showed that the SSE values were lower for the camera with the cooled detector. McMillan [14] measured the SSE for both an LWIR camera and an MWIR camera, each at a single radiant temperature. Since the objective was the radiometric calibration of the cameras, the SSE was not systematically investigated to assess the influence of optical elements, the detection wavelength range, or other factors. The modulation transfer function (MTF) of the thermal imaging system was used to describe the SSE in uncooled detector cameras [2,15]. According to Budzier and Gerlach [2], the deviation from the ideal behaviour indicates that lower MTF values lead to a reduction in contrast resulting in SSE. However, Schramm et al. [15] noted that a single MTF measurement cannot fully describe all the root causes involved, such as sensor element crosstalk and residual errors in non-linearity correction, among others.

This research presents a study of the size-of-source effect on a heterogeneous configuration of infrared cameras (see Table 1). Analysis is performed at different radiant temperatures on the detection range, the optical configuration, and the detector pitch. The measured behaviour is compared with the behaviour of an analytical model formulated from a measured MTF. The paper is structured as follows: Section 2 describes the Methodology, including cameras studied, the experimental setup, and the method used to evaluate the SSE. The results are presented and discussed in Section 3 presents and discussed the experimental results. Finally, Section 4 presents the conclusions and provides an outlook on the work planned in the near future.

Table 1. Technical data of the studied cameras. The specified measurement ranges are divided into subgroups that can be selected for each camera. UC stands for uncooled.

Specification	Unit	Camera 1	Camera 2	Camera 3	Camera 4
Spectral range	μm	7.5 to 14	7.5 to 13	3.2 to 3.4	2.0 to 5.7
Detector format $W \times H$	px	640 × 480	382 × 288	320 × 240	640 × 512
FOV	°	30 × 23	62 × 49	24 × 18	5.5 × 4.4
Detector pitch a	μm	25	25	30	15
f/F	mm/-	30/1	8/0.8	23/1.5	100/3.0
Measurement range	°C	−40 to 1200	−20 to 900	−40 to 350	−40 to 3000
Uncertainty	–	$\pm$ max(1.5K, 2%*ofreading*) or 2 %	$\pm$2K*or* $\pm$ 2% r $\pm$2 %	$\pm$ max(1K, 2%*ofreading*) or $\pm$2 %	$\pm$ max(1K, 1%*ofreading*) or $\pm$1 %
NETD @30	mK	<30	<40	<25	<25
Detector element	–	UC microbolometer	UC microbolometer	Cooled InSb	Cooled InSb

2. Methodology

As mentioned above, the SSE is a systematic measurement error that is unavoidable for infrared optical systems. In this paper, the SSE is studied for a group of thermal imaging cameras at different radiant temperature set points T_{set}. The objective is to assess how the configuration of the thermal imaging system, expressed by detector technology and optical components, influences the SSE and how the SSE depends on the temperature. This section describes the considerations taken for the experimental setup and the measurement procedure to ensure that the observed deviations were only associated with the SSE.

2.1. Experimental setup

For the present work, the radiometric calibration of the cameras is not under consideration, but the dependence of the measured temperature on the size of the radiating object is examined. The proper execution of the calibration is assumed, but the limitation of the procedure due to the use of constant geometry is evaluated. This dependency was measured with the aid of a plate radiator and circular apertures. The radiant source must provide well-defined temperature values with sufficient temporal stability and a spatially homogeneous response. Moreover, it must allow full irradiation of the detectors of all four cameras in the vertical direction to capture the possible range of object sizes under laboratory conditions. Circular apertures must be designed and manufactured to ensure thermal images with sufficient contrast. Their sizes must be chosen to obtain representative and comparable measurements from each camera.

2.1.1. Thermal imaging cameras

A heterogeneous group of four cameras was selected for this study. The first two cameras (camera 1 & 2) operate in the LWIR with a uncooled microbolometer detector and different optical objectives. Camera 1 is equipped with a normal optical lens, while camera 2 uses a fisheye optical lens. Cameras 3 & 4 both operate in the MWIR. However, camera 3 is equipped with a spectral filter designed to capture radiance in a specific narrow band of the spectrum, which is utilised for the visualisation of gases. This camera uses a standard optical lens, while camera 4 is fitted with a telescopic lens. These technical details, as well as complementary information, are listed in Table 1.

2.1.2. Apertures

Circular geometric patterns made from 2 mm stainless steel sheets were used for the study. This material was chosen because it is a good heat conductor and facilitates a homogeneous temperature distribution on the side facing the camera. This side was coated with a certified paint to increase the emissivity value of the surface facing the infrared cameras, and thus prevent the capturing of reflected radiation from objects in the surroundings. According to the paint manufacturer, an emissivity value of $\varepsilon > 0.9$ is assured in the LWIR and MWIR [16]. The opposite side was left unpainted. Due to the low emissivity of stainless steel $\varepsilon < 0.3$ the infrared radiation coming from the plate radiator is mainly reflected, slowing the heating of the metal sheet. If the temperature of the aperture increases, the modulation introduced by the experimental setup will be reduced, resulting in deviations that could not be totally associated with the SSE of the cameras. An increase in aperture

temperatures was also reported by Pušnik et al. [10], who implemented an active cooling of the apertures using a water circuit. The holes were laser-cut to provide a smooth surface finish without burrs along the circumference. Additionally, cutting tools introduce a conical pattern around the edges of small-diameter holes, which is not reproducible for larger diameter apertures. An exemplary sample is presented in Figure 1.

Circular geometry was preferred because it allows for symmetry along axes oriented in any direction. If a different geometry had been chosen, such as a triangle or a rectangle, the behaviour of the diffracted energy would have depended on the direction. SSE deviations obtained with circular apertures were compared to those produced with rectangular slits by Ohtsuka and Bedford [3]. For a slit width x, the measured SSE was approximately the same as that for a circle with a diameter of $2 \cdot x$. The authors argued that the very long slit diffracts about twice the energy into the focal beam, whereas the diffraction from the circular aperture is limited in all directions.

The four cameras were compared using a dimensionless diameter:

$$\phi_{\text{rel}} = \frac{\phi_{\text{px}}}{H} \tag{1}$$

where ϕ_{px} refers to the diameter obtained in the image in pixel units and H is the vertical resolution of the camera. The diameters of the apertures and the measurement distances were selected to produce a comparable distribution of ϕ_{rel} for the four cameras. The smallest diameter in all cases was limited to 10 pixels, since the magnitude response of optical systems at high spatial frequencies drops drastically [2]. Pušnik et al. [11] also suggested that the SSE should be measured at least in a region of interest (ROI) of 10 px $\times$ 10 px. Table 2 lists the diameters and distances used for the measurements with each camera. The diameters obtained in the images ϕ_{px} were calculated considering the distance D_{CA} between the edge of the camera lens and the painted surface of the apertures. The design of the apertures ensured the alignment of the centres of the manufactured circles with the centre point of the heat plate radiator when positioned.

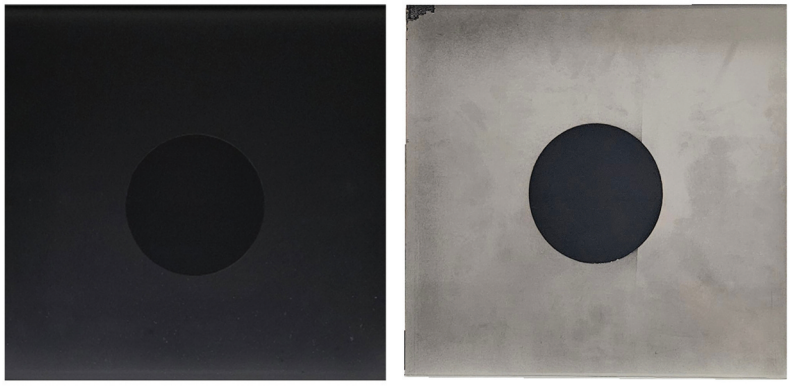

Figure 1. Metal sheet apertures. The side facing the cameras and the side facing the heat plate radiator are presented in (a) and (b), respectively.

Table 2. Distances and diameters considered for the evaluation of the SSE.

Camera	Distance D_{CA} in mm	Aperture diameters ϕ in mm	Aperture diameters ϕ_{px} in px	Relative diameters ϕ_{rel} in %
1	458	{8, 15, 25.4, 35, 50, 75, 100, 122, 140, 168}	{21, 39, 66, 91, 131, 196, 261, 319, 366, 439}	{4, 8, 14, 19, 27, 41, 54, 66, 76, 91}
2	150	{8, 15, 25.4, 35, 50, 75, 100, 122}	{17, 32, 54, 74, 106, 158, 211, 257}	{6, 11, 19, 26, 37, 55, 74, 89}
3	441	{8, 15, 25.4, 35, 50, 75, 100, 122, 132}	{14, 26, 44, 61, 87, 130, 173, 211, 229}	{6, 11, 19, 25, 36, 54, 72, 88, 95}
4	1920	{8, 15, 25.4, 35, 50, 75, 100, 122, 140}	{28, 52, 87, 120, 172, 258, 344, 419, 481}	{5, 10, 17, 23, 34, 50, 67, 82, 94}

2.1.3. Heat plate radiator

The radiant source commissioned for the measurement of the SSE is a heat plate radiator IR-150/301 manufactured by Infrared Systems [17]. The radiant energy is emitted from a Black flat square surface of 12 inches $\times$ 12 inches, with an emissivity of $\varepsilon = 0.96 \pm 0.02$ in a wavelength range of $1 - 99\,\mu m$. The plate radiator operates from ambient temperature up to 500°C. The manufacturer states a spatial non-uniformity of about $\pm 1\% T_{set}$ for a centred area of 10 inches $\times$ 10 inches, and a temporal stability in the short (long) term of $\pm 0.1°C$ $(\pm 0.2°C)$. The device is operated with an active Multi-Band PID controller, whose control action is limited to increase the surface temperature, since the radiator is not equipped with a cooling system.

2.1.4. Measuring stand

The measuring stand was designed for the purpose of measuring the SSE of thermal imaging cameras, in various optical configurations, so as to be reproducible and reliable. The stand is presented in Figure 2. The heat plate radiator (label 1 – rectangle with red dotted lines in Figure 2(c)) was mounted on a rigid frame, which also serves as a cabinet for the controller (label 2) and the apertures (label 4). These are inserted into a grooved profile (label 5) and then pressed with screws (rectangle with orange dotted lines in Figure 2(a)), so that the apertures do not tilt with respect to the Black body surface (Black dashed line in Figure 2(b,c)).

The original housing (label 3) was modified to enable a wider range of the distance D_{AB} between the position of the apertures and the Black body radiator surface. The presence of the aperture affects the dynamics of convective heat transfer between the emitting surface and the environment, which the controller regulates. However, the side of the aperture facing the radiator plate (Figure 1(b)) reflects the radiation coming from the Black body surface, which is again absorbed by this high-emissivity surface. This results in a sudden increase in the surface temperature. Since these devices are not specifically designed for measuring the SSE, the response of the device is not fast enough to counteract the effects associated with the positioning of the apertures. This implies that the measuring stand and the data acquisition must be planned in such a manner that, as long as the SSE is measured, the thermal behaviour in front of the Black body radiator surface remains as close as possible from the steady-state condition without an aperture in front.

To evaluate the disturbance in the thermal equilibrium of the heat plate radiator caused by the presence of the aperture, the temporal evolution of the temperature in the defined region of interest (see Section 2.3) was monitored. The experiment involved sequential testing of four apertures with varying sizes ϕ_{rel}, arranged from smallest to largest. The procedure was as follows: First, the smallest aperture was placed in front of the heat plate radiator and held in place for 10 seconds. Subsequently, the aperture was removed and the radiator was left unobstructed for two minutes to allow the system to return to thermal equilibrium.

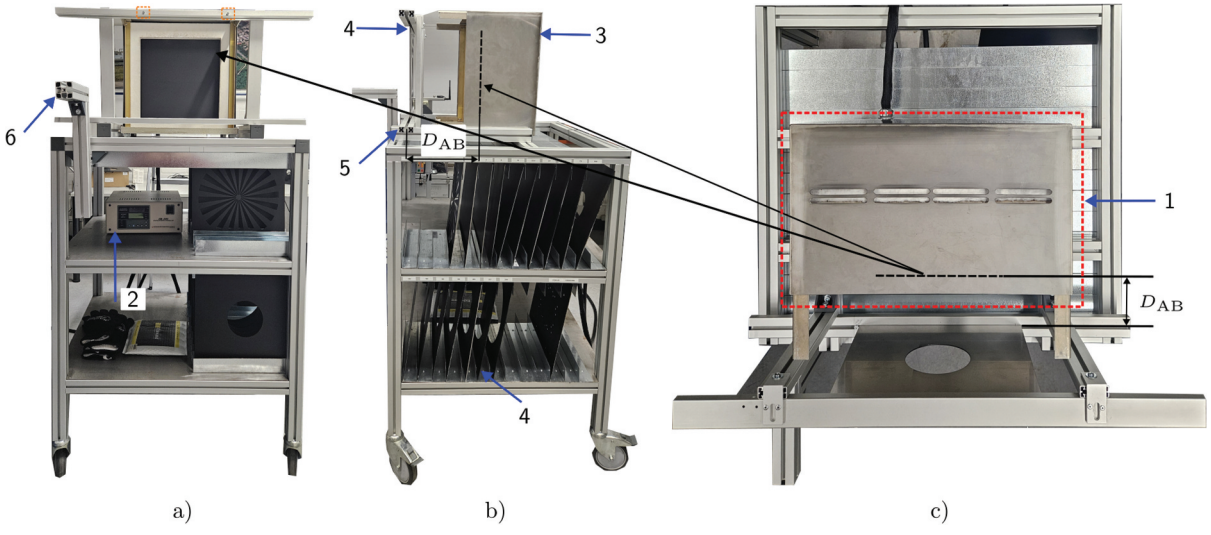

Figure 2. Measurement stand. The front, side, and top views are shown in (a), (b), and (c) respectively. The heat plate radiator is indicated with label 1, the controller with label 2, the manufactured housing with label 3, the metal apertures with label 4, the aperture holder with label 5 and the auxiliary arm for positioning the cameras with label 6.

This process was repeated for the remaining apertures, with each positioned in front of the radiator for 10 seconds, followed by a two-minute recovery period.

This experiment was conducted using Camera 4, configured to capture 10 frames per second, recording continuously. The controller of the heat plate radiator was set to $T_{set} = 523.15$ K which is the highest temperature considered for this study (see Section 2.2). This condition represents the worst-case scenario of the disruption caused by the apertures to the thermal equilibrium. Four distances, D_{AB}:

$$D_{AB} \in \{80, 170, 250, 300\} \text{ in mm}$$

were selected for the study to determine the point at which the SSE can be isolated from other potential thermal effects caused by the presence of the aperture. The distance values were determined by the constructive limits of the measurement stand. Figure 3(a) presents the instantaneous temperature deviation $\Delta\theta_i^n$:

$$\Delta\theta_i^n = \theta_i^n - \theta_{ref} \tag{2}$$

where i is the i-th aperture (see Section 2.3), n denotes the time index, and θ_i^n represents the instantaneous mean temperature value obtained in the region of interest shown in Figure 5 (see Section 2.3). The reference temperature θ_{ref} is calculated for each distance D_{AB} as the temporal average of the instantaneous temperature values of the heat plate surface (θ_{BB}^n) when no aperture is present. This value is determined from a circular region of interest (ROI) with a 10 px diameter, centred on the thermogram.

$$\theta_{ref} = \frac{1}{N}\sum_{n=1}^{N} \theta_{BB}^n \tag{3}$$

with N being the number of thermograms, for which the heat plate surface was set free. It can be observed in Figure 3(a) how the presence of the apertures affects the dynamics of the radiating plate, as seen in the fluctuations before and after the positioning of the apertures. Before the placement of the apertures, the oscillation of $\Delta\theta_{BB}^n$ around 0 K ($\Delta\theta_{BB}^n = \theta_{BB}^n - \theta_{ref}$) is of the same order as the temporal stability indication given by the heat plate manufacturer (see Section 2.1.3). When the apertures are placed, θ_i^n varies the most for the shorter distance ($D_{AB} = 80$), and is more stable as the D_{AB} increases, showing little significant change for the two longer distances (see error bars in Figure 3(b). After the apertures are removed, the control action of the controller is observed and the steady state of the temperature is again achieved after a short period.

Figure 3(b) illustrates the absolute temperature deviations calculated with (4), where θ_i is the average value of the temperature calculated for time intervals of 10 seconds when the i-aperture was placed, and θ_{ref}

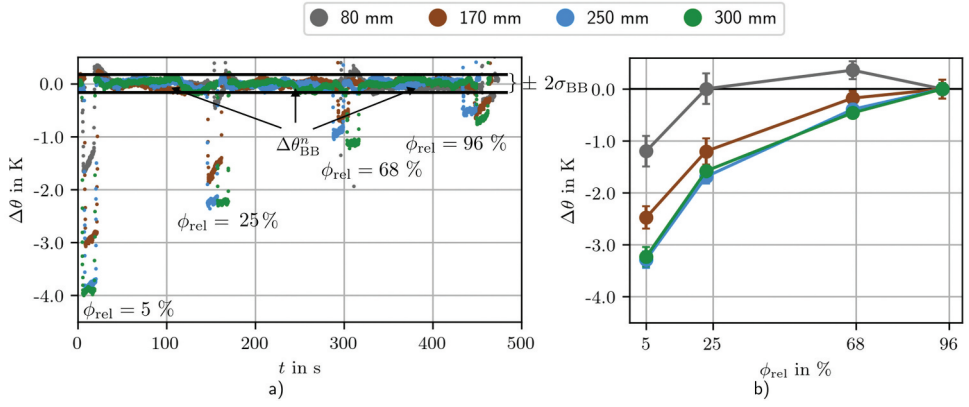

Figure 3. Temperature deviations measured at four different distances D_{AB} for $T_{set} = 523.15$ K using camera 4, with a sampling rate of 10 frames per second. The temporal evolution of the temperature deviations $\Delta\theta_i^n$ is calculated with (2) and presented in (a). σ_{BB} is the temporal standard deviation of θ_{BB}^n, which varies from 0.13 to 0.16 K for the four analyzed distances. In this case, the reference temperature θ_{ref} is the mean temperature value when the surface of the calibrator was unobstructed. The temperature deviation $\Delta\theta$ is presented in (b), with θ_{ref} calculated with the mean temperature value for the aperture with $\phi_{rel} = 96\%$ placed in front of the calibrator. The error bars represent two temporal standard deviations of the measured temperature for each diameter.

is equivalent to the largest aperture $\phi_{rel} = 96\%$ ($\theta_{ref} = \theta_{96}$). The circular markers on the plot correspond to $\Delta\theta_i$, and the error bars correspond to two temporal standard deviations obtained from θ_i^n. Monotonic curves are obtained for $D_{AB} \geq 170$ mm. For $D_{AB} = 80$ mm the obtained behaviour could be attributed to a sudden increase in temperature produced by the reflected radiation, which counteracts the temperature differences associated with the SSE. This effect is proportional to the exposed aperture area to the heat plate radiator, which decreases with the square of the diameter aperture. For $\phi_{rel} = 96\%$ this reflection effect is not as dramatic for the temperature control, but the curve progression is not monotonic since at this aperture the reference temperature is set. For $D_{AB} = 170$ mm, the progression is monotonic, but the temporal variations are of the same order as for $D_{AB} = 80$ mm. For $D_{AB} = 250$ mm and $D_{AB} = 300$ mm, a superposition of the curves is observed and the temporal variation is similar in both cases. Considering both aspects, it can be inferred that the disruption of the thermal equilibrium caused by the presence of the apertures is not significant for distances D_{AB} between $250-300$ mm, and the measurements at these distances capture mainly the phenomena associated with the SSE.

For the present study, the measurements were performed at $D_{AB} = 250$ mm, since the White borders around the radiator plate (see Figure 2(a)) become visible in the image of the camera 2 further than this distance. For the data acquisition, the cameras 1, 3 & 4 were mounted on tripods. Camera 2 was positioned with the help of a movable auxiliary arm (label 6), since the prescribed distance D_{CA} could not be configured with a tripod.

2.2. Data acquisition

The SSE was studied for three radiant temperature set points T_{set}:

$$T_{set} \in \{323.15, 393.15, 523.15\}\ \text{K}$$

For each T_{set}, the measurements were conducted 40 minutes after obtaining the temperature in steady state on the controller display, according to the manufacturer indications to ensure a homogeneous surface temperature distribution of the Black body surface. The camera under investigation was placed in front of the infrared calibrator, and the optical centre was aligned with the centre of the largest aperture.

The focus was set at the centre of the image with a 15° slanted edge aperture (see Figure 4), in order to have the same focus configuration as for the MTF measurement (see Section 2.4).

The non-uniformity correction was performed before the acquisition of the thermograms for each temperature set point with the help of a finn board at room temperature. The cameras with a microbolometer detector were exposed to the plate radiator only for the measurement of the SSE, to prevent heating of the sensor, which would introduce cross-talk between the microbolometer cells.

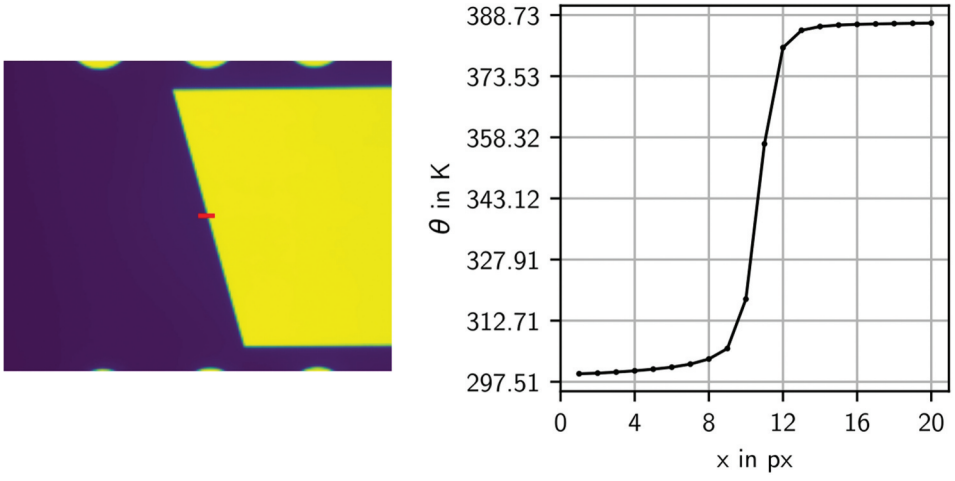

Figure 4. Focus adjustment with the slanted edge. The temperature profile over the red line in (a) is presented in (b).

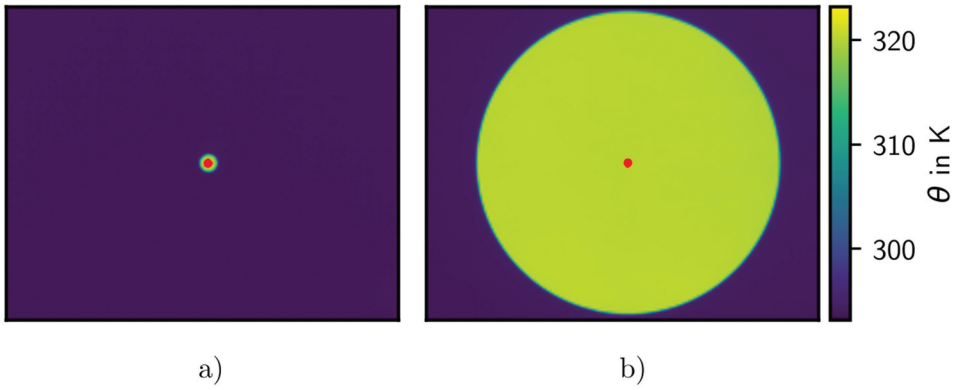

Figure 5. Thermograms of the apertures with the smallest (a) and widest circle (b) obtained with the camera 4. The ROI is depicted in both cases as the red region.

The thermograms were collected immediately after the apertures were placed, to prevent performing the measurements while the surface temperature was being altered by the apertures themselves. The acquisition of the thermograms was separated into time intervals of 2 minutes, to achieve the thermal equilibrium again. The measurement sequence for all cameras and for T_{set} proceeded from the smallest diameter to the largest. A sequence of 50 consecutive images was obtained for each measurement point, which were then averaged to obtain a representative value over the sampling period.

The ambient temperature and the relative humidity were measured to monitor the experimental conditions and to correct the deviations associated with the air transmittance, especially for camera 4 due to its large measurement distance D_{CA}. These values, in conjunction with the emissivity of the plate radiator, were entered into the cameras' software modules to perform the respective corrections.

2.3. Size-of-source effect assessment

The SSE is evaluated for the complete set of apertures in a region of interest (ROI), defined as a concentric circular region (see Figure 5). The diameter of the ROI was fixed at 10 px to ensure a consistent assessment of the SSE over a similar area of the heat plate in each case. The coordinates of the centre and the radius of the circle were obtained using the digital image processing algorithm *HoughCircles* of the *OpenCV* library [18].

For each aperture, an absolute temperature deviation $\Delta\theta_i$ is calculated:

$$\Delta\theta_i = \theta_i - \theta_{ref} \tag{4}$$

where θ_i refers to the mean temperature value in the ROI for the i-th aperture, and θ_{ref} is the value obtained at the largest aperture for each camera, as indicated in the German technical guideline VDI/VDE 5585 Part 1 – Section 4.27 [1].

Radiance values were also considered for assessing the SSE. This was done through the numerical integration of the Planck's law:

$$L(\lambda,\theta) = \int_{\lambda_1}^{\lambda_2} \frac{2hc_0^2}{\lambda^5\left(\exp\left(\frac{hc_0}{\lambda k\theta}\right)-1\right)} d\lambda \tag{5}$$

where h is the Planck constant, c_0 is the speed of light in a vacuum, λ is the wavelength and k is the Stefan-Boltzmann constant. With this, the absolute difference ΔL_i and the relative deviation $L_{rel,i}$ are defined as follows:

$$\Delta L_i = L_i - L_{ref} \tag{6}$$

and,

$$L_{rel,i} = \frac{L_i}{L_{ref}} \tag{7}$$

where L_i and L_{ref} correspond to the radiance values calculated from θ_i and θ_{ref}. $\Delta\theta_i$ measures the temperature deviation experienced by the user, ΔL_i represents the radiation that does not reach the corresponding area of the ROI in the detector, and $L_{rel,i}$ indicates how the degradation varies with the object size, using a reference point.

2.4. Modulation transfer function

The imaging process of infrared cameras can be modelled through the theory of linear opto-electronic systems, in which the smallest detail that can be represented by an optical system is described by the point spread function (PSF). Given an ideal irradiance object distribution $i(x,y)$, the PSF maps the response of the system from each object point source into the real irradiance distribution $u(x,y)$:

$$u(x,y) = i(x,y) * PSF(x,y) \tag{8}$$

For the ideal case, the $PSF(x,y)$ acts as a delta-impulse response, yielding the best possible representation of the object in the image [19]. For real infrared systems, the optical behaviour is limited by Fraunhofer diffraction and aberrations [20]. Therefore its impulse response, the PSF, has a defined spatial extent, rather than being a point. In the frequency domain, the object irradiance distribution can be represented as a composition of various spatial frequencies by means of Fourier analysis. Taking the Fourier transform $\mathcal{F}$ of each side of (8):

$$U(f_x,f_y) = I(f_x,f_y) \cdot OTF(f_x,f_y) \tag{9}$$

where f_x and f_y are spatial frequencies in x and y directions, and OTF is the optical transfer function. As a complex function, the OTF has a magnitude and a phase portion:

$$OTF(f_x,f_y) = MTF(f_x,f_y)e^{jPTF(f_x,f_y)} \tag{10}$$

with the modulation transfer function MTF and the phase transfer function PTF. If the PSF is symmetric and centred on the ideal image point (on focus), and has no temporal components, which is the assumed case for this paper, the PTF has a value of zero and the OTF is completely described by the MTF.

In consideration of the aforementioned, the MTF is a subject of considerable interest to optical system manufacturers, and methods to measure it have been developed. One such method is the slanted-edge method, presented by the International Organization for Standardization [21] and considered for this work, which consists of recreating a knife-edge image, e.g. Figure 4(a), to calculate the edge spread function (ESF). The first derivative of the ESF in a given direction leads to the line spread function (LSF), describing the transfer behaviour in one direction. In order to arrive at the MTF, the LSF must be normalised and Fourier-transformed:

$$D(f_x) = \mathcal{F}\{LSF(x)\} = \mathcal{F}\{\frac{d}{dx}(ESF)\} \tag{11}$$

and then:

$$MTF(f_x) = \frac{D(f_x)}{D(f_x = 0)} \tag{12}$$

The horizontal MTF was measured with the described method using a slanted-edge with an 15° angle. This angle was selected to combine four pixel rows to obtain the super-sampled ESF. The signal-to-noise ratio was improved by obtaining the mean value of the ESFs enclosed in the ROI, which was set to capture the behaviour close to the optical centre of the cameras, a region in which the SSE is measured. The heat plate radiator was set at $T_{set} = 393.15$ K, in order to guarantee a suitable modulation depth [22]. Figure 6 shows the calculation process of the MTF.

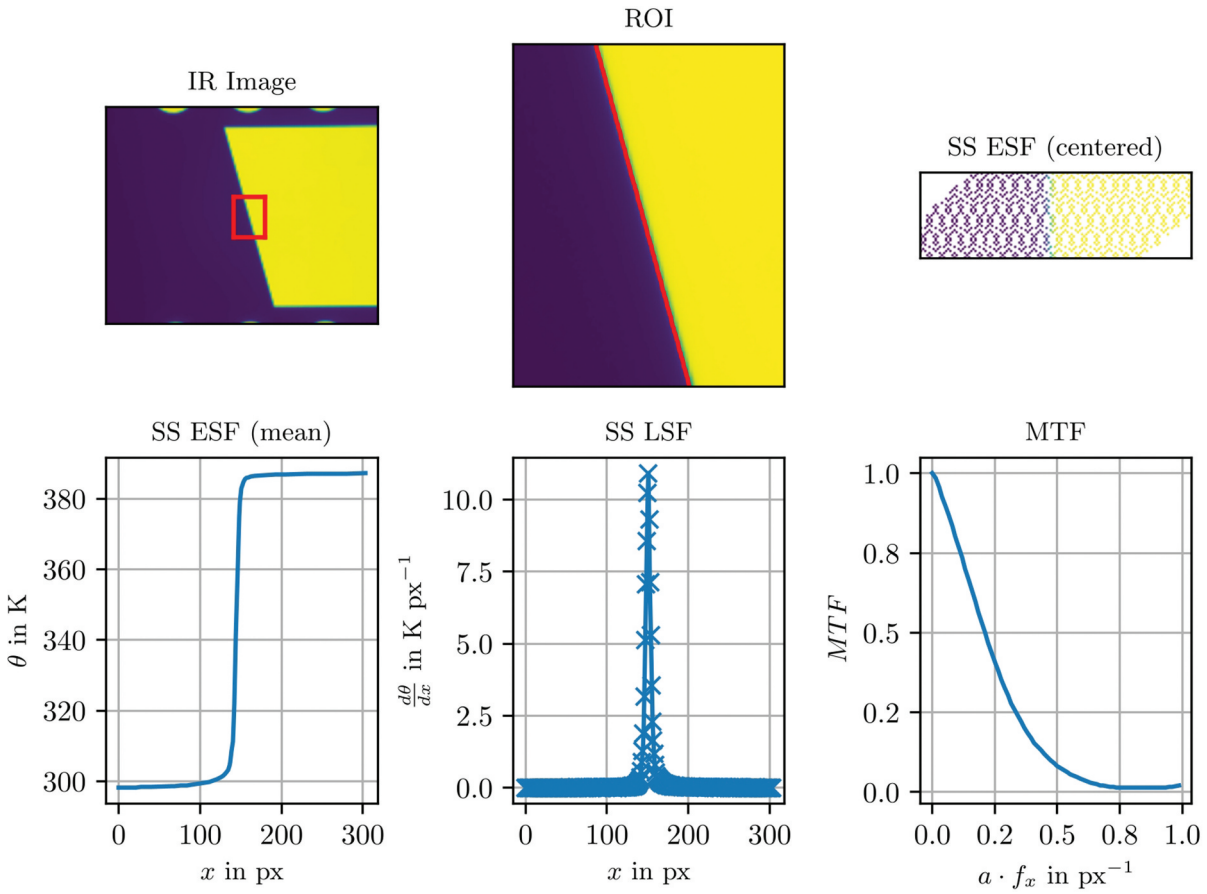

Figure 6. Measurement example of the MTF obtained with the camera 4. A ROI (red square) is selected in the slanted-edge thermogram that is selected, from which the ESF is super sampled (SS). This is then averaged in the vertical direction and differentiated to calculate the LSF. The MTF is obtained from the Fourier transform of the LSF, where the discontinuities are first removed using a Hann window.

3. Results and discussion

The results are discussed regarding two main topics: The relationship between the SSE, the radiant temperature, and the correspondence of the MTF with the SSE.

3.1. Relationship between the size-of-source effect and the radiant temperature

The measured and calculated temperature and radiance deviations $\Delta\theta$ and ΔL are presented in Figure 7. In all cases, the curves are mainly monotonic. The greatest deviation, referred to the largest diameter aperture, is observed for the smallest aperture, and it increases with the temperature. Punctual disruptions are observed in the curve courses, which could be associated with insufficient measurement of the SSE, especially when the measurement conditions were not fully met despite strict adherence to the prescribed measurement procedure. However, this behaviour could be also attributed to post-processing of the obtained signal, e.g. temperature drift compensations, which are performed by the cameras' software. Nevertheless, since the values themselves are not the most pertinent for the study, but the trends expressed in the curves, the results represent the behaviour of the SSE for the prescribed conditions.

A clear difference between the values of $\Delta\theta$ for both LWIR cameras is observed when compared to those for both MWIR cameras. This difference is also evident for the curves of ΔL which show a dramatic contrast between the two spectral ranges. This can be attributed to the impact that optical performance has on the resulting deviations, highlighting the relevance of this factor for each spectral range. To analyse this, the fractional change in exitance of a blackbody due to a fractional change in temperature can be calculated with (13) [23], which is described as follows:

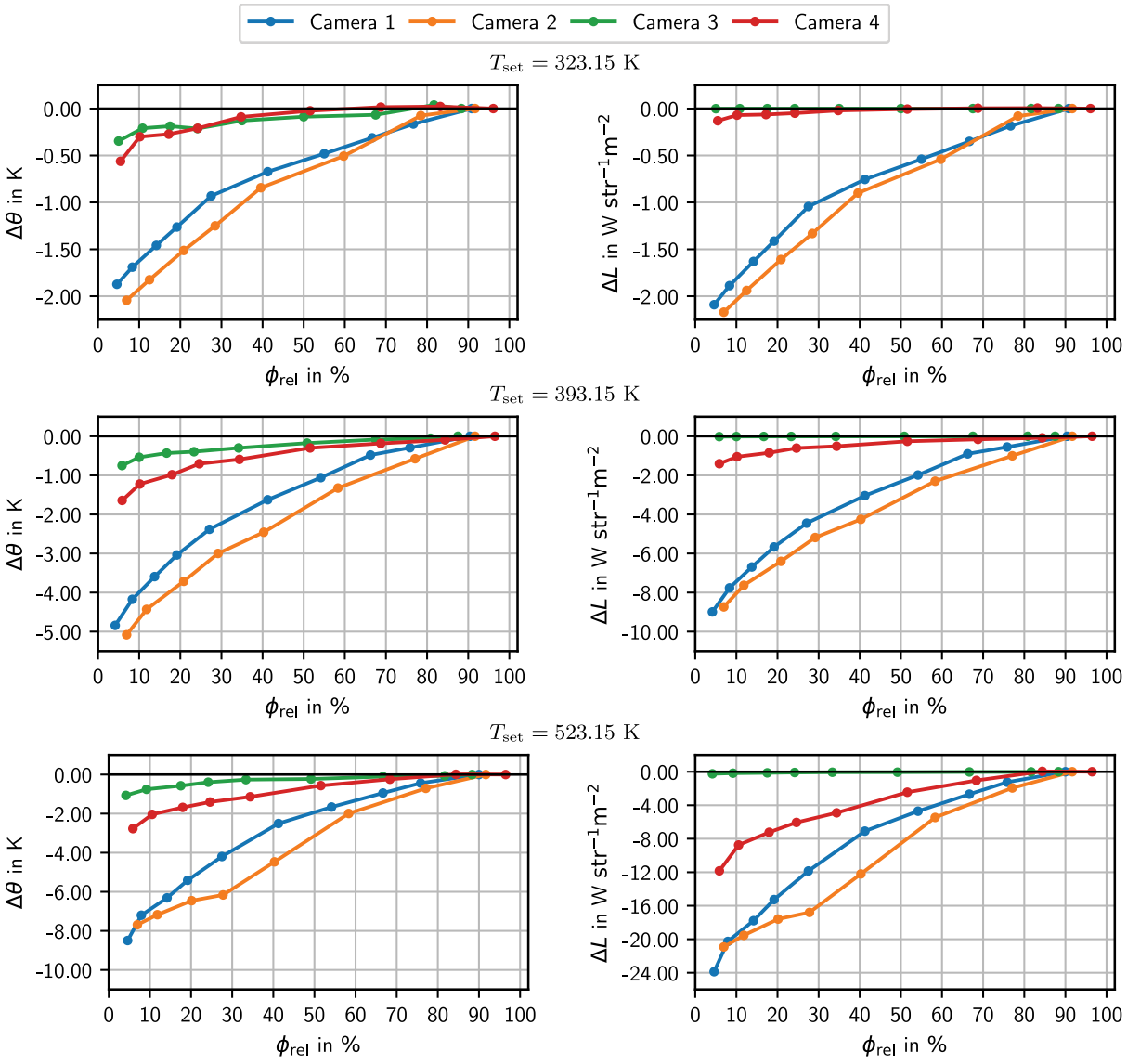

Figure 7. Calculated $\Delta\theta$ and ΔL.

$$P(\lambda,\theta) = \frac{\frac{dM_\lambda(\theta)}{M_\lambda(\theta)}}{\frac{d\theta}{\theta}} = \frac{c_2}{\lambda\theta}\frac{\exp(\frac{c_2}{\lambda\theta})}{\exp(\frac{c_2}{\lambda\theta}) - 1} \tag{13}$$

where M corresponds to the spectral exitance and $c_2 = hc/k$ is the second radiant constant. The change of detector signal can then be estimated with (13). Assuming that unavoidable effects on the optical components are measured through the measured temperature deviation $\Delta\theta_{mess}$, the relative change of the detector signals R can then be calculated as:

$$R = \frac{\Delta L_{detector}}{L_{obj}} = \frac{L_{obj} - L_{mess}}{L_{obj}} = P\,\frac{\Delta\theta_{mess}}{\theta} \tag{14}$$

The effective irradiance on the detector is then:

$$L_{mess}(\lambda,\theta) = L_{obj}(1 - R) \tag{15}$$

For an exemplary case with camera 1 (LWIR) and camera 4 (MWIR), P and R were calculated for the radiant temperatures T_{set} considered in this paper, listed in Table 3. According to the results, for a relative change of 1% in the object temperature the relative change in the MWIR detector signal is at least 2.57 times greater than the equivalent for the LWIR detector, but the relative change of the signal detector R is similar in both

Table 3. Estimated change in detector signal with the temperature in LWIR and MWIR. The calculations were conducted with centre wavelength approximation (Camera 1 $\lambda_{LWIR} = 10.75$ and Camera 4 $\lambda_{MWIR} = 3.85$).

T_{set} in K	P_{LWIR}	P_{MWIR}	P_{MWIR}/P_{LWIR}	R_{LWIR}	R_{MWIR}
323.15	4.21	11.56	2.74	2.47	2.14
393.15	3.52	9.50	2.69	4.48	4.35
523.15	2.77	7.15	2.57	4.50	3.14

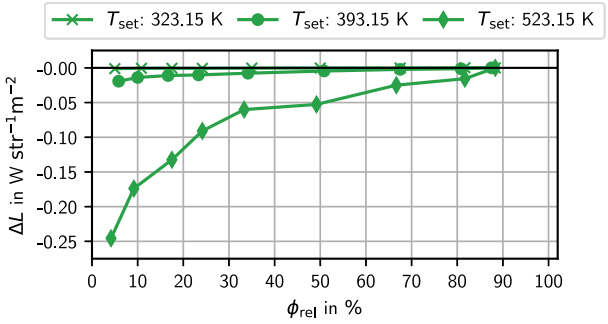

Figure 8. Calculated ΔL for three temperature set points. The minimum value of ΔL observed for $T_{set} = 323.15$ K is $\Delta L = -1.17 \times 10^{-3}$W str^{-1}m^{-2}.

cases, at least for $T_{set} = 323.15$ K and $T_{set} = 393.15$ K. Figure 9 presents the relationship between the loss in the detector input signal and the resulting temperature difference for $T_{set} = 393.15$ K. For the LWIR camera, R results in larger radiance and, consequently, larger temperature deviations compared with the MWIR camera.

The calculated curves for L_{rel} support this statement, where the greater deviations (up to 5 %) are observed for the LWIR cameras (see Figure 10). Regarding the camera 3 & 4, the difference between the experimental results could be associated with the narrow sensitive spectrum of the camera 3 detectors. Meanwhile, $|\Delta\theta|$ for the camera 4 increases to 3, for the camera 3 was bounded under 1, for all three radiant temperature set points. This is clearly visible in the calculated ΔL curves (see Figure 8) and L_{rel} curves (see Figure 10) for the camera 3, which shows the smallest deviation in all cases.

In Figure 10 a superposition of the corresponding curves of the cameras 1, 2, and 4 is observed for $T_{set} = 393.15$ K and $T_{set} = 523.15$ K. Machin and Ibrahim [4] reported an overlap in L_{rel} curves for the SSE measured above a radiant temperature of ($T_{set} \geq 373.15$ K), and smaller deviations below this temperature, as it is seen in this work. The authors suggested there is not a strong link of the radiant temperature value

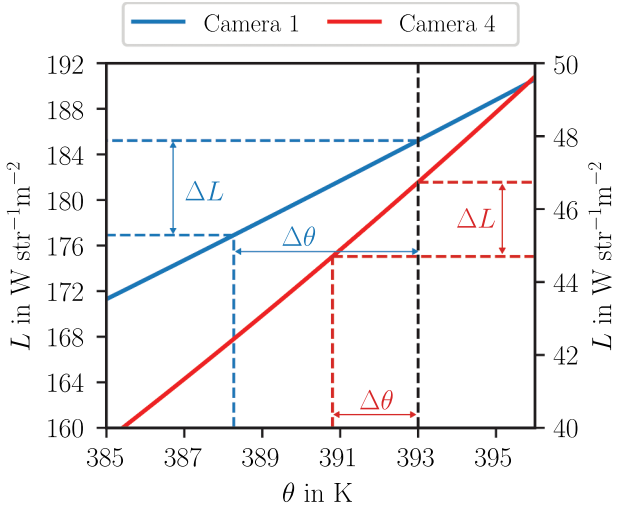

Figure 9. Relationship between the loss in the detector input signal and the resulting temperature difference at $T_{set} = 393.15$ K (Black dashed line), for camera 1 (left axis) and camera 4 (right axis).

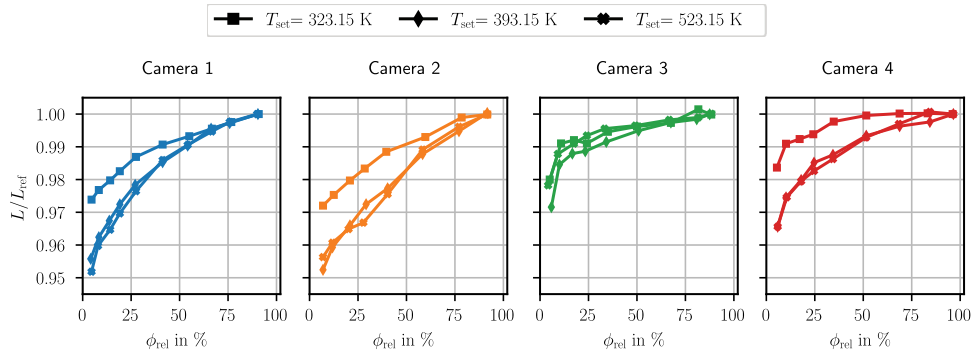

Figure 10. Calculated values of L_{rel}.

with the SSE, specially for the cases in which the background temperature is negligible compared to the radiant temperature. For the camera 3 this is not clearly observed. Since this camera operates in a very narrow spectral range, the calculated differences were very small and the method used may not guarantee sufficient accuracy. McMillan [14] suggested that the SSE of a temperature-invariant sensor can be measured using the method described by Bloembergen [24]. This method will be explored in future studies to assess its applicability to infrared cameras.

3.2. Modulation transfer function and size-of-source effect

The MTF measurements for all cameras are presented in Figure 11. For comparison, the dimensions of the ROI, considered for the calculation of the MTF, were normalised with the image dimensions. For the horizontal direction x:

$$\mathrm{ROI}_{\mathrm{rel},x} = \frac{\Delta x_{\mathrm{ROI}}}{H} \cdot 100 \tag{16}$$

where Δx_{ROI} corresponds to the horizontal dimension of the ROI. For the vertical direction, the calculations are performed with Δx_{ROI} and the normalisation factor is V. Table 4 presents the normalised ROI for the four cameras.

The curves for cameras 2, 3, and 4 exhibit similar behaviour, while camera 1 shows a distinct double curvature change in the frequency range f_x between 10 and 20 mm^{-1}. This observation was confirmed through additional MTF measurements, which yielded the same result.

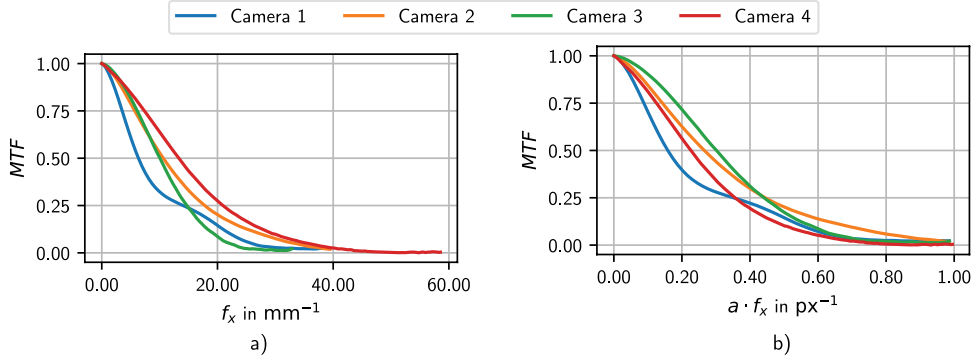

Figure 11. Measured MTF.

Table 4. Dimensions of the normalised ROI for the MTF calculation.

	Camera 1	Camera 2	Camera 3	Camera 4
$\mathrm{ROI}_{\mathrm{rel},x}$ in %	10.62	17.80	22.50	11.71
$\mathrm{ROI}_{\mathrm{rel},y}$ in %	25.20	27.80	35.00	18.55

The measured MTF represents the magnitude of the opto-electrical system's response to sinusoidal signals at different spatial frequencies [19]. According to Budzier and Gerlach [2], in a thermal camera, the MTF is the product of the optical system's response and the detector's response, which is ultimately restricted by the pixel width. The measurements demonstrate how higher spatial resolution promotes better object sampling, leading to improved modulation depth. This results in the system MTF being limited by the pixel MTF [2], which is especially observed for the camera 3. To decouple the spatial response and analyse the optical system's behaviour, the spatial frequency was multiplied by the pixel width, as shown in Figure 11(b). It becomes evident that the measured MTF is similar for both camera groups (LWIR and MWIR) in this representation; an evaluation of the MTF values does not explain why the measured deviations differ markedly in both cases. Budzier and Gerlach [2] stated that the SSE can be explained by the MTF through the contrast reduction caused by the optics. If a similar reduction in the modulation depth occurs, this is more evident for the LWIR cameras, which results in greater temperature deviations in LWIR (see Section 3.1). The results also revealed that, if the cameras are compared by spectral range, a larger focal length improves the modulation depth, consistent with the theory of diffraction-limited lenses [2,19].

The SSE measurements were compared against the prediction of the analytical model:

$$L_{\mathrm{Out}} = L_{\mathrm{In}} * LSF(x) \tag{17}$$

where L_{In} is the ideal measuring scene and L_{Out} is the image retrieved by the thermal imaging camera, both in radiance units. The calculated radiance level L_{in} is obtained from a temperature profile θ_{in}, considered as an ideal rectangular signal:

$$\theta_{in}(x) = \begin{cases} \theta_{\mathrm{inf}} & if|x| \leq \frac{\phi_{px}}{2} \\ \theta_{ap} & if|x| > \frac{\phi_{px}}{2} \end{cases}$$

where θ_{ap} is the temperature of the aperture, assumed to be at room conditions $\theta_{\mathrm{ap}} = 295.15$ K, and θ_{inf} is a theoretical reference value corresponding to a temperature measured from an object with infinite dimensions. This consideration was made to provide an unbiased criterion for the comparison between the value predicted by the model and the one measured with the thermographic cameras. The calculation of θ_{inf} was performed from the mathematical limit of a functional form proposed by Bloembergen [25], which establishes a mathematical relationship for the measured temperature deviations $\Delta\theta$:

$$\Delta\theta = -\mathrm{A} \cdot \exp(-\mathrm{B} \cdot \phi_{\mathrm{rel}}) + \mathrm{C} \tag{18}$$

where the coefficients A, B and C are calculated from a standard regression problem. The coefficient C provides a degree of freedom for better adjusting of the curves [25] and the limit to the infinity of his functional form approaches to this value:

$$\lim_{\phi_{\mathrm{rel}} \to \infty} \Delta\theta(\phi_{\mathrm{rel}}) = \mathrm{C} \tag{19}$$

The theoretical temperature θ_{inf} for $\phi_{\mathrm{rel}} \to \infty$ is then:

$$\theta_{\mathrm{inf}} = \theta_{\mathrm{ref}} + C \tag{20}$$

Figure 12(a) presents a comparison example for the camera 4, between the temperature profiles obtained from (17) (blue) and the measured thermogram delivered by the thermographic camera (green). It can be noticed that the model reproduces the behaviour produced by the optics of the camera along the progression of the temperature profile. The measured, adjusted and predicted temperature deviations for cameras 1 & 4 at a radiant temperature of $T_{\mathrm{set}} = 393.15$ K are presented in Figure 12(b,c), respectively. It is observed that, when moving from right to left, the predicted temperature deviations remain nearly constant and close to zero, but then decrease sharply starting at $\phi_{\mathrm{rel}} = 18\%$. This suggests that the model's predictions are primarily evident for small aperture diameters.

In order to address this, the temperature deviations $\Delta\theta$ were recalculated using the reference temperature at the smallest aperture to highlight the differences from this point. Furthermore, $\Delta\theta$ was normalised by the difference between θ_{inf} and θ_{ap} to facilitate comparison with the ideal modulation:

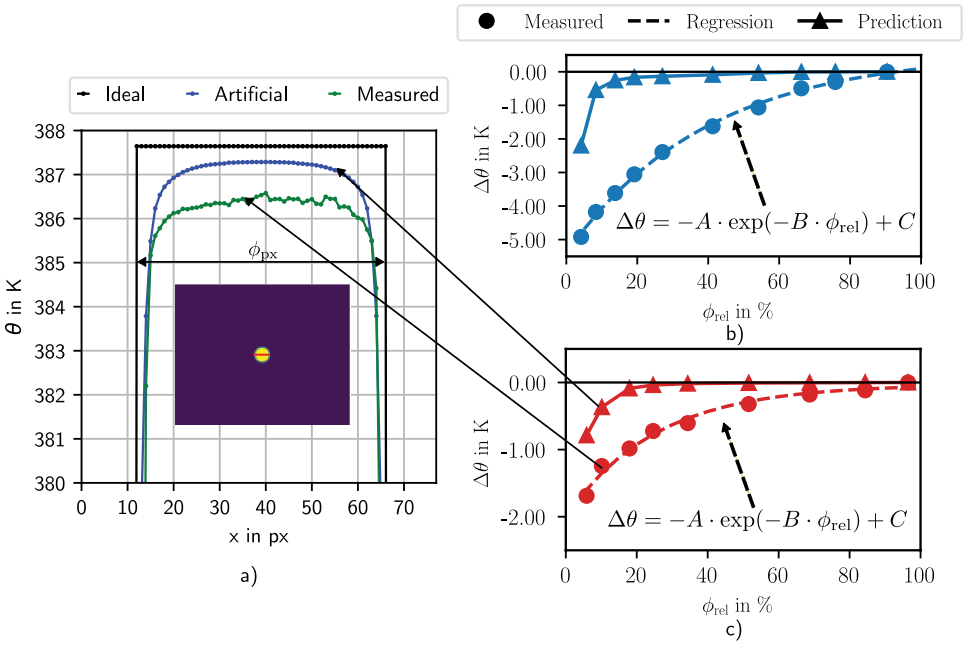

Figure 12. Comparison of the SSE predicted by the MTF model and direct measurements. The exemplary temperature profiles for camera 4, obtained along the red line from the ideal, artificial, and measured thermograms, are presented in a). The temperature deviations $\Delta\theta^*$ for cameras 1 and 4 are shown in b) and c), respectively. The coefficient C of the adjusted functional form (see (18)) described by Bloembergen [25], is $C_1 = 0.57$ K and $C_4 = 0.26$ K.

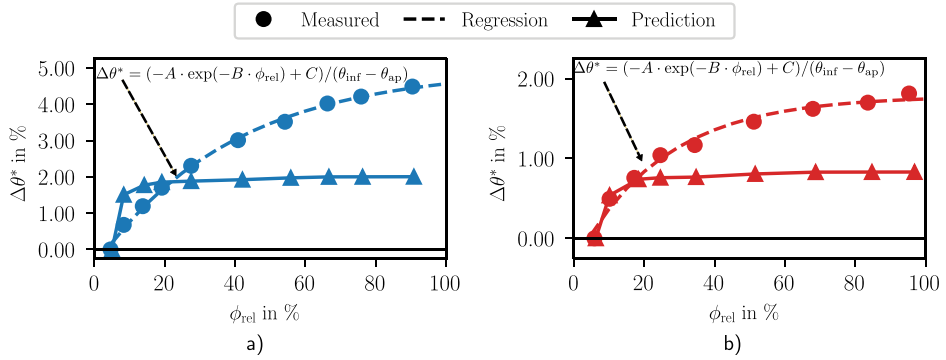

Figure 13. Comparison between the SSE predicted by the MTF model and direct measurements. The temperature deviations originally presented in Figure 12(b,c) were recalculated using θ_{ref} set at the smallest aperture to highlight the model's predictions for smaller object sizes. The newly calculated temperature differences were normalized according to (21) and are shown in a) and b), respectively.

$$\Delta\theta^* = \Delta\theta / (\theta_{inf} - \theta_{ap}) \tag{21}$$

Figure 13 presents the recalculated and normalised temperature deviations $\Delta\theta^*$ corresponding to Figure 12(b,c). This new representation shows that, for camera 4, the steep progression observable up to $\phi_{rel} = 18\%$ aligns well with the results of the SSE measurements. Conversely, although the model for camera 1 captures the temperature deviations resulting from contrast reduction at high frequencies, its predictions lack precision. This imprecision is linked to the measured MTF and the underlying model, which is based on a one-dimensional MTF measurement, so effects captured in two-dimensional measurements may be missed by the 1D-based model.

Nevertheless, the increasing temperature deviations observed in the experimental results are not reflected in the model predictions, which converge from $\phi_{rel} = 18\%$ onwards. This suggests that the model effectively captures the behaviour for small object sizes–at least for camera 4—but struggles with

larger ones due to insufficient sampling at low frequencies in the MTF measurement. This limitation restricts the model's ability to predict the SSE in this region of the spatial spectrum.

The convergence of temperature deviations was also addressed by Ohtsuka and Bedford [3]. The authors compared the predictions of a mathematical model for diffraction-limited optical systems with SSE measurements. Although the model predicted the same shape of the curves, it failed to capture the ongoing increase in deviation after a point referred to as the 'knee' of the curves. To evaluate the influence of other phenomena not included in the model formulation, such as scattered light, the authors conducted a series of separate experiments. They demonstrated that a reduction in the transmittance of the scattering medium has the greatest impact on deviations for larger diameters, compared to smaller ones. The effect of scattered light was analysed by depositing varying amounts of chalk dust and re-measuring the SSE. Results showed that the increase in SSE, as a function of source diameter, was amplified in proportion to the amount of chalk deposited, especially at larger diameters. Conversely, for curves corresponding to partially and fully cleaned lenses, the rate of change in measured deviations with increasing diameter remained almost constant in the latter case. Based on these observations, Ohtsuka and Bedford [3] concluded that the differences observed for larger radiant sources are primarily due to scattering, while diffraction remains virtually constant.

The description of optical systems, which are affected not only by diffraction limits but also by geometric aberrations and surface scattering effects, is addressed through the derivation of a composite MTF by Harvey [26]. According to him, the formulation of a system based on linear systems theory is feasible, provided that the degradation mechanisms are independent and uncorrelated. Different contributions to the MTF, such as motion, vibration, turbulence, and the presence of aerosols can be included through a cascade-multiplication approach, as Boreman [19] suggested.

The model proposed by Harvey [26] involves the construction of a surface transfer function (STF), which primarily depends on the ratio between the average surface roughness and the wavelength, which is then multiplied by the diffraction-limited MTF. The results show that the STF undergoes a sudden change at low spatial frequencies, where the measured MTF lacks to describe the SSE, and remains constant across the higher frequencies. With this consideration, the SSE should be better described from the theory across the entire object size range. This approach will be further investigated in future studies to refine the mathematical model for describing the SSE and to address the underestimation observed in fully diffraction-limited models, as reported by Ohtsuka and Bedford [3] and corroborated in this work.

4. Conclusion and outlook

The SSE was measured and assessed for two LWIR cameras (1 & 2) and two MWIR cameras (3 & 4), each with different optical configurations. The analysed variables showed monotonic trends in temperature and radiance deviations. The largest difference, associated with the largest aperture diameter, was observed for the smallest diameter and increased with higher radiant temperatures. A clear distinction was noted between the analysed spectral ranges, where the SSE of the cooled MWIR cameras was significantly lower. The relative radiance curves overlapped for temperatures $T_{set} = 393.15$ K and $T_{set} = 523.15$ K. This behaviour was also observed in radiant thermometers, where the curves for each radiant temperature overlapped as the difference between the radiant temperature and the thermocouple temperature increased. This suggests that the SSE can be measured as temperature-invariant for a given optical system of an infrared camera, provided that background radiation is negligible or corrected.

The system response of the thermography cameras was assessed to compare the predicted SSE deviations obtained with an analytical approach. To achieve this, the horizontal diffraction-limited modulation transfer function (MTF) was measured using the slanted-edge method. The results highlighted the effects of improved spatial resolution and different lens types. The response of the cameras to an ideal irradiance signal input was simulated and compared with the SSE measurements. It was observed that the analytical approach can reproduce the optical response on the temperature profiles but fails to capture the measured temperature deviations caused by the SSE. This may be associated with the measured MTF, which does not account for all events related to the SSE, as its estimation is based on a one-dimensional measurement. Moreover, these underestimations could be associated with additional effects, such as scattering, not accounted for by the measured MTF. This suggests that the proposed model delivers a rough approximation

of the actual SSE and can be improved by performing a 2D measurement of the MTF and including the aforementioned effects. These considerations should reduce the discrepancy between the model predictions and actual measurements.

In future work, the effect of optical configurations on SSE will be systematically evaluated. For a fixed camera, the SSE will be measured with different optical objectives and various neutral density filters. The theoretical model will be formulated in 2D and extended to include terms associated with optical scattering and compared with the SSE measured for each configuration. Additionally, the experimental setup will be enhanced with the use of an iris diaphragm, which is expected to reduce measurement effort and increase the volume of data collected, providing valuable insights for mathematical modelling. Finally, higher radiant temperatures, up to $T_{set} = 773.15$ K, will be considered to assess the behaviour of the SSE at different radiation levels.

Disclosure statement

No potential conflict of interest was reported by the author(s).

Funding

This work is supported by the Bundesministerium für Wirtschaft und Klimaschutz (BMWK) on the basis of a decision by the German Bundestag under Grant: [KK5055007AB1].

ORCID

Miguel-David Mendez-Bohorquez http://orcid.org/0009-0009-9168-747X

References

[1] VDI/VDE-Gesellschaft Mess- und Automatisierungstechnik (GMA). VDI/VDE 5585 Part 1. Technical temperature measurement -Temperature measurement with thermographic cameras – metrological characterization. Verein Deutscher Ingenieure; 2018.
[2] Budzier H, Gerlach G. The size-of-source effect in thermography. J Sens Sens Syst. 2021;10(2):179–184. doi: 10.5194/jsss-10-179-2021
[3] Ohtsuka M, Bedford R. Measurement of size-of-source effects in an optical pyrometer. Measurement. 1989;7(1):2–6. doi: 10.1016/0263-2241(89)90019-5
[4] Graham M, Mohamed I. SSE and Temperature uncertainty. II-Low temperature systems. In: Dubbeldam J, de Groot MJ, editors. The 7th International Symposium on Temperature and Thermal Measurements in Industry and Science. Vol. II. Delft: NMi Van Swinden Laboratorium in cooperation with Technical Committee 12 of the International Measurement Confederation IMEKO, 1999. p. 687–692.
[5] Graham M, Gennady S. A comparative study of size of source effect (SSE) determination techniques. In: Fellmuth B, Seidel J, Scholz G, editors. 8th International Symposium on Temperature and Thermal Measurements in Industry and Science. Vol. 1. Berlin. VDI/VDE-Gesellschaft Mess- und Automatisierungstechnik (GMA); 2001. p. 150–160.
[6] Bart M, Van Der Ham EWM, Saunders P. A new method to determine the size-of-source effect. Int J Thermophys. 2007;28(6):2111–2117. doi: 10.1007/s10765-007-0251-6
[7] Saunders P, Edgar H. On the characterization and correction of the size-of-source effect in radiation thermometers. Metrologia. 2008;46(1):62–74. doi: 10.1088/0026-1394/46/1/008
[8] Yoon HW, Allen DW, Saunders RD. Methods to reduce the size-of-source effect in radiometers. Metrologia. 2005;42(2):89–96. doi: 10.1088/0026-1394/42/2/003
[9] Hill KD, Woods DJ. Exploring the size-of-source and distance effects of radiation thermometers. In: Zvizdic D, Grgec Bermanec L, Stasic T, Veliki T, editors. 9th International Symposium on Temperature and Thermal Measurements in Industry and Science. Vol. 1. Cavtat-Dubrovnik. Laboratory for Process Measurement; 2004. p. 599–604.
[10] Pušnik I, Grgić G, Drnovšek J. System for the determination of the size-of-source effect of radiation thermometers with the direct reading of temperature. Meas Sci Technol. 2006 June;17(6):1330–1336. doi: 10.1088/0957-0233/17/6/007
[11] Pušnik I, Geršak G. Evaluation of the size-of-source effect in thermal imaging cameras. Sensors. 2021;21(2):1–22. doi: 10.3390/s21020607
[12] Schramm S, Schmoll R, Kroll A. Compensation of the size-of-source effect of infrared cameras using image processing methods. In: 13th International Conference on Sensing Technology (ICST); Sidney. IEEE; 2019. p. 1–6.

[13] König S, Gutschwager B, Taubert RD, et al. Metrological characterization and calibration of thermographic cameras for quantitative temperature measurement. J Sens Sens Syst. 2020;9(2):425–442. doi: 10.5194/jsss-9-425-2020
[14] McMillan J. Traceable thermal imaging in harsh environments [PhD thesis]. University of Surrey; 2023.
[15] Schramm S, Ebert J, Schmoll R, et al. Compensating the size-of-source effect: relationship between the MTF and a data-driven convolution filter approach. In: Maldague X, editor. 16th Quantitative InfraRed Thermography Conference (QIRT); Organizing Committee of the Conference QIRT 2022 (Paris, France). Québec - Canada; 2022. p. 1001.
[16] Lab IR Paints. Thermographic paint for low temperature applications. [cited 2024 May 9]. Available from: https://paints.labir.cz/en/paints/herp-lt/
[17] Infrared Systems Development Corporation. IR-150/301 blackbody system. [cited 2024 May 9]. Available from: https://www.infraredsystems.com/Products/blackbody150.html
[18] Bradski G. The OpenCV library. Dr Dobb's J Softw Tools. 2000;25:120–125.
[19] Boreman GD. Modulation transfer function in optical and electro-optical systems. 2nd ed. Bellingham (WA): SPIE Press; 2021.
[20] Budzier H, Gerlach G. Thermal infrared sensors: theory, optimisation and practice. Chichester (UK): Wiley; 2011.
[21] International Organization for Standardization (ISO). ISO 12233: 2017. Photography - electronic still picture imaging - resolution and spatial frequency responses. International standard, 2017.
[22] Homassel E, Barrat C, Alves F, et al. Improved modulation transfer function evaluation method of a camera at any field point with a scanning tilted knife edge. In: Hickman DL, Bürsing H, editors. Electro-optical and infrared systems: technology and applications xvii. Vol. 11537. Bellingham (WA): International Society for Optics and Photonics, SPIE; 2020. p. 115370B.
[23] Vollmer M, Möllmann K. Infrared thermal imaging: fundamentals, research and applications. Weinheim (Germany): Wiley-VCH Verlag GmbH & Co. KGaA; 2017.
[24] Bloembergen P. On the correction for the size-of-source effect corrupted by background radiation. In: The 7th International Symposium on Temperature and Thermal Measurements in Industry and Science: NMi Van Swinden Laboratorium in cooperation with Technical Committee 12 of the International Measurement Confederation IMEKO Delft; 1999. p. 607–612.
[25] Bloembergen P. Analytical representations of the size-of-source effect. Metrologia. 2009;46(5):534–543. doi: 10.1088/0026-1394/46/5/018
[26] Harvey J. Parametric analysis of the effect of scattered light upon the modulation transfer function. Opt Eng. 2013;52(7):073110. doi: 10.1117/1.OE.52.7.073110